

Article

Study on the Head Loss of the Inlet Gradient Section of the Aqueduct

Jian Chen , Yangyang Tian, Huijie Zhang and Shanju Zhang *

School of Water Conservancy, North China University of Water Resources and Electric Power, Zhengzhou 450046, China

* Correspondence: zhangshanju@ncwu.edu.cn; Tel.: +86-185-3876-0918

Abstract: The form of the inlet section of aqueducts that connect the upstream channel and the downstream channel affects the flow pattern and head loss. In order to provide a reference for the design of the gradient section of water-transfer channels, a typical three-dimensional hydrodynamic model is established in this paper based on existing results. The results show that the local head loss coefficient is related to the cross-sectional area of the inlet and outlet of the gradient section, the water surface contraction angle of the gradient section, and the elevation difference between the bottoms of the inlet and outlet of the gradient section, and a functional relationship is provided; when changing the width of the inlet and outlet bottoms, the local head loss coefficient is negatively related to the water surface contraction angle and increases with the increase in W_{up}/W_{down} ; the local head loss coefficient has a good exponential function with W_{up}/W_{down} . The research results can provide a reference for the design of the inlet gradient section and the solution of the head loss coefficient.

Keywords: transition channel; numerical simulation; local head loss coefficient; transition channel inlet gradient section



Citation: Chen, J.; Tian, Y.; Zhang, H.; Zhang, S. Study on the Head Loss of the Inlet Gradient Section of the Aqueduct. *Water* **2023**, *15*, 1633. <https://doi.org/10.3390/w15081633>

Academic Editors: Wan Hanna Melini Wan Mohtar and Zohreh Sheikh Khozani

Received: 8 March 2023

Revised: 5 April 2023

Accepted: 19 April 2023

Published: 21 April 2023



Copyright: © 2023 by the authors. Licensee MDPI, Basel, Switzerland. This article is an open access article distributed under the terms and conditions of the Creative Commons Attribution (CC BY) license (<https://creativecommons.org/licenses/by/4.0/>).

1. Introduction

Aqueducts are important water crossing structures that mainly consist of three parts: the inlet transition section, the tank body section, and the outlet transition section, and are widely used in water transmission projects. When the inlet transition section is too short, the cross-sectional area decreases sharply and the turbulence of the water flow increases, or the water flow changes from slow flow to rapid flow, which inhibits the flow capacity.

The problem of local head loss in the constriction section of the channel has been studied by many researchers. Nguyen et al. [1] measured the local head loss coefficient for the transition from a rectangular channel to a pressurized pipe by means of physical model tests, and the local head loss coefficient was $\zeta = 0.63 (1 - \text{downstream cross-sectional area}/\text{upstream cross-sectional area})$ when the constriction section was symmetrical. The hydraulic calculation manual [2] and the design specifications of irrigation and drainage canal system buildings [3] provide some empirical head loss coefficients without providing a clear correlation between them. Zhai Yuanjun [4] designed and conducted increased flow tests on several typical channel transition section models, and performed regression analysis to obtain a one-dimensional quadratic function relationship between the local head loss coefficient and the contraction angle. Wu Yongyan et al. [5] conducted a physical model test study on the flow characteristics of a transition section from a trapezoidal open channel to a horseshoe unpressurized tunnel and obtained the relationship between the local loss coefficient and the area ratio between the upper and lower reaches of the constriction section and the bottom elevation difference. Wang Songtao [6] and Qu Zhigang [7] revealed the mechanism of water surface fluctuation in the trough body of the aqueduct by numerical model simulation of a typical aqueduct in the South–North Water Transfer Central Line. Kazemipour and Apelt [8] reported that, when the transition section changes dramatically,

the local head loss can even account for more than 90% of the total head loss. Local head loss can be calculated by multiplying the velocity head rate by the local head loss coefficient, and the reasonable selection of the local head loss coefficient is key to the correct estimation of local head loss. The local head loss coefficient generally needs to be selected according to the form of the transition section, Henderson [9] pointed out that, when the transition section forms from an abrupt change to a gradual change, the local head loss coefficient can be reduced by two-thirds; Chow [10] suggested a local head loss coefficient of 0.1–0.2 for a twisted surface form of a transition section, 0.3–0.5 for a linear form, and 0.75 for an abrupt change. Yaziji [11] measured a local head loss coefficient of 0.2–0.42 for linear and streamlined shrinkage transition sections. Zhang Zhiheng [12] reported that, for twisted surface transition sections, the local head loss coefficient of the tunnel inlet is not a constant, but is related to the shrinkage angle of the water's surface. Crispino Gaetano et al. [13] conducted calibrated numerical simulations to assess the hydraulic features of supercritical bend manholes with variable deflection angles, curvature radii, and lengths of straight downstream extension elements. It was demonstrated that the hydraulic capacity of a bend manhole increased with increased curvature radii and straight extension lengths, whereas the effect of the deflection angle was less significant. Cheng Yong et al. [14] studied the three-dimensional flow at the open channel bifurcation by numerical simulation using FLOW-3D software, analyzed the hydraulic characteristics of the recirculation zone and flow structure near the open-channel bifurcation, and obtained the equations for the inflow width of the surface and bottom layers in a trapezoidal channel. Tellez-Alvarez, J et al. [15] studied the energy loss coefficients of three types of grate. The energy losses recorded at flow rates between 20 L/s and 50 L/s ranged between 0.15 and 3.41, showing a negative correlation. It is known that it is feasible to study the hydraulic characteristics of aqueducts using the three-dimensional numerical simulation method.

Based on the Flow-3D software platform, this paper conducts a numerical simulation of a typical aqueduct in the South–North Water Transfer Central Project to study the factors influencing the head loss coefficient of the inlet gradient section.

There are no clear formulas for calculating head loss in existing studies and codes, or the factors affecting head loss have been considered to be small. In order to highlight the influence of head loss factors, this paper, based on existing research, considers the influence of the water surface contraction angle, inlet and outlet overwater area, and water level difference of the gradient section and downstream water depth, and provides the calculation formula for the head loss of the gradient section to support the engineering design.

2. Establishment of Mathematical Model

2.1. Model Layout

The total length of a typical section of the South–North Water Diversion Central Project is 660 m, the designed flow is 350 m³/s, the designed water level at the inlet is 146.801 m, and the designed water level at the outlet is 146.491 m. The increased flow is 420 m³/s, the increased water level at the inlet is 147.561 m, and the increased water level at the outlet is 147.211 m. The available head for design flow is 0.31 m. The parameters connecting the upstream channel of the aqueduct are the top elevation of the bottom plate (138.801 m), the bottom width (19 m), the internal slope (1:2), and the longitudinal slope ($i = 1/25,000$). The parameters of the downstream channel are the top elevation of the bottom plate (138.491 m), the bottom width (19 m), the internal slope (1:2), and the longitudinal slope ($i = 1/25,000$).

The transition section at the entrance and exit of the aqueduct is a twisted surface structure. The Rhino drawing software has high accuracy for the establishment of the surface and was used to establish the three-dimensional calculation model of the aqueduct. In consideration of the influence of the inlet and outlet boundary conditions on the numerical simulation results, 200 m trapezoidal channel sections were set up upstream and downstream of the inlet and outlet transition sections of the aqueduct.

The established three-dimensional model of the aqueduct was established according to the 1:1 model scale. The X-axis direction was selected as the left and right bank direction,

with the right bank direction as the X-axis positive direction, the Z-direction was the water depth direction, with the Z-axis negative direction being the gravitational acceleration direction, and the Y-axis was the upstream and downstream direction, with the Y-axis positive direction being the downstream flow direction. As shown in Figures 1 and 2, the total length of the model was 941 m, including 541 m for the aqueduct and 200 m for the inlet and outlet channel sections.

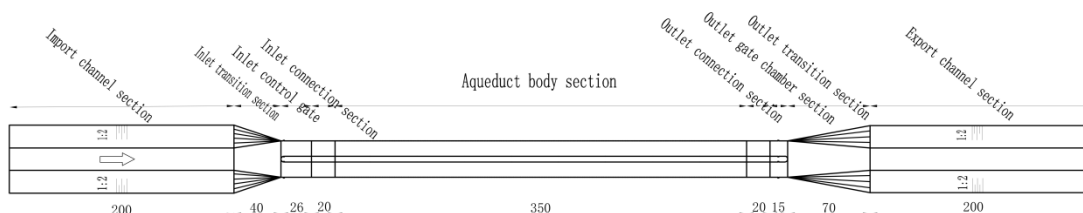


Figure 1. Aqueduct floor plan.



Figure 2. Three-dimensional layout of the aqueduct.

2.2. Governing Equation

The software takes the Navier–Stokes equation as the control equation and uses the Reynolds average method to solve it [16].

Continuity equation:

$$\frac{\partial}{\partial x_i} (u_i A_i) = 0 \tag{1}$$

Momentum equation:

$$\frac{\partial u_i}{\partial t} + \frac{1}{V_F} \left(\sum_{j=1}^3 u_j A_j \frac{\partial u_i}{\partial x_j} \right) = -\frac{1}{\rho} \frac{\partial P}{\partial x_i} + g_i + f_i \tag{2}$$

where u_i is the direction speed of X, Y, and Z. A_x , A_y , and A_z are the area of the calculation unit of direction; V_F is the volume fraction of water in each calculation unit; ρ is the density of water; P is the pressure; g_i is gravity; and f_i is the Reynolds stress [17].

Turbulence model:

For RNG k- ϵ , the model can efficiently solve the flow with large streamline bending [18].

Turbulent kinetic energy equation:

$$\frac{\partial(\rho k)}{\partial t} + \frac{\partial(\rho u_i k)}{\partial x_i} = \frac{\partial}{\partial x_j} \left((\mu + \mu_t) \alpha_k \frac{\partial k}{\partial x_j} \right) + G_k - \rho \epsilon \tag{3}$$

Turbulent energy dissipation rate equation:

$$\frac{\partial(\rho \epsilon)}{\partial t} + \frac{\partial(\rho u_i \epsilon)}{\partial x_i} = \frac{\partial}{\partial x_j} \left((\mu + \mu_t) \alpha_\epsilon \frac{\partial \epsilon}{\partial x_j} \right) + C_{1\epsilon}^* \frac{\epsilon}{k} G_k - C_{2\epsilon} \rho \frac{\epsilon^2}{k} \tag{4}$$

where k is the turbulent kinetic energy, ϵ is the turbulent energy dissipation rate, μ is the hydrodynamic viscosity coefficient, μ_t is the fluid turbulent viscosity, $\mu_t = \rho C_\mu k^2 / \epsilon$, $N \cdot s / m^2$; α_ϵ , α_k , $C_{1\epsilon}$ and B are constants; $\alpha_\epsilon = \alpha_k = 1.39$; $C_{1\epsilon}^* = C_{1\epsilon} - \eta(1 - \eta/\eta_0) / (1 + \beta\eta^3)$; $\eta = (2E_{ij}E_{ij})^{0.5} k / \epsilon$; $E_{ij} = 1/2(\partial u_i / \partial x_j + \partial u_j / \partial x_i)$ $\eta_0 = 4.337$; $\beta = 0.012$; $C_{1\epsilon} = 1.42$;

constant $C_{2\varepsilon} = 1.68$; and G_k is the turbulent kinetic energy generation term caused by the average velocity gradient, $G_k = \mu_t(\partial u_i/\partial u_j + \partial u_j/\partial u_i)\partial u_i/\partial u_j$ [19].

2.3. Model Meshing

In this paper, the FLOW-3D software 11.2 was used for meshing, and the mesh was a hexahedral mesh corresponding to the six faces of the 3D model. FLOW3D draws meshes that are divided into structural meshes. It also uses the FAVOR technology to check whether the meshes can be accurately identified with the computational model.

The quality of grid division affects the accuracy of numerical model calculation results. In order to improve the accuracy of the numerical simulation results and to consider the calculation time, the mesh can be optimized and the calculation time costs can be reduced, provided that the results are accurate.

(1) Grid irrelevance test

In this paper, the irrelevance of a uniform grid with five grid widths of 1.0, 0.9, 0.8, 0.7, and 0.6 m was tested. The grid shape was square. The water depth at the middle of the inlet of the inlet gradient section (point A) was selected for analysis. The numerical simulation results are shown in Table 1.

Table 1. Simulation results for different grid widths.

| Grid Width/m | Total Number of Grids | Number of Fluid Grids | Ending Time/s | Approximate Time of Stabilization/s | Simulated Water Depth at Point A/m |
|--------------|-----------------------|-----------------------|---------------|-------------------------------------|------------------------------------|
| 1.0 | 765,000 | 426,400 | 5000 | 3000 | 8.236 |
| 0.9 | 987,400 | 545,700 | 5000 | 3000 | 8.203 |
| 0.8 | 1,395,000 | 771,000 | 5000 | 3000 | 8.185 |
| 0.7 | 1,915,500 | 1,045,700 | 5000 | 3000 | 8.183 |
| 0.6 | 2,729,400 | 1,440,900 | 5000 | 3000 | 8.181 |

As can be seen from Table 1, when the grid size is larger than 0.8 m, the grid width has a greater influence on the simulation results, and the smaller the grid size, the smaller the change in the simulation results; when the grid size is smaller than 0.8 m, the grid width has less influence on the simulation results. Therefore, for the sake of time and accuracy, the grid width in this paper was 0.8 m.

(2) Grid division

The model was divided following the non-uniform grid method, the important parts of the model were nested, and the local grid was densified. The hydraulic characteristics of the inlet and outlet transition sections were the focus of this paper. Nested grid processing was carried out for the positions of the entrance and exit transition sections and the vicinity of the middle pier of the exit transition section. The nested grid of the model exit transition section area is shown in Figure 3. The nested grid area of the exit transition section was as follows: X axis (−10 m–10 m), Y axis (650 m–741 m), Z axis (−2.5 m–9.76 m), and the grid division size was 0.5 m. The nested grid area of the entrance transition section was as follows: X axis (−10 m–10 m), Y axis (200 m–260 m), Z axis (−2.5 m–9.76 m), and the grid size was 0.5 m. The overall mesh size was 0.8 m and the total number of grids was 1.395 million.

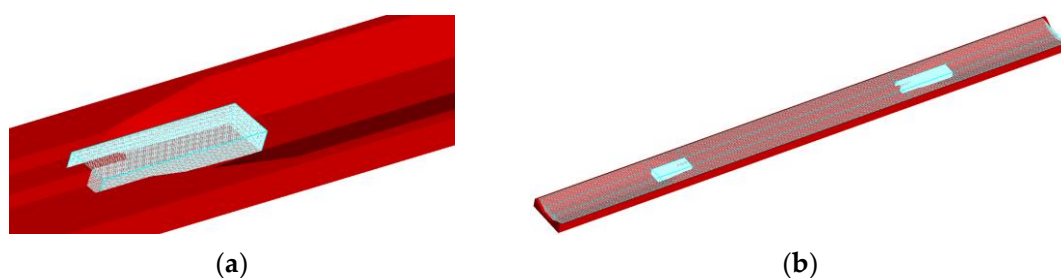


Figure 3. Grid division. (a) Export gradient segment local encryption; (b) Model meshing.

2.4. Setting of Model Boundary Conditions and Initial Conditions

(1) Boundary condition setting

The upstream inlet boundary condition of the model was set as the flow inlet boundary. The downstream outlet boundary condition of the model was set as the pressure outlet boundary, and the water level corresponding to each simulated working condition was provided. The wall boundary was provided at the left and right banks (positive and negative directions of the X -axis) and at the bottom of the model (negative direction of the Z -axis). The pressure outlet was provided at the top of the model (positive direction of the Z -axis), where the fluid fraction was set to 0; that is, the top of the model was atmospheric pressure.

(2) Initial condition setting

It can be seen from Figure 2 that the total length of the calculation model was 941 m. If the initial conditions of the model do not provide the corresponding initial water level according to the simulation conditions, and the tank runs empty, the calculation time will be increased. If only the initial water level is given, the water flow in the tank will oscillate during the simulation, and it will take a long time for the model to stabilize, therefore, on the basis of the given water level, an average flow rate is provided for the initial water body according to the simulation conditions to reduce the oscillation and improve the calculation efficiency. In order to clearly and accurately determine the stability of the model calculation, monitoring sections were set up upstream and downstream of the inlet and outlet to observe the flow and velocity changes of specific sections. When the difference between the instantaneous changes in flow is very small, the model calculation is stable [20].

3. Model Validation

3.1. Comparison of Measured Data of Model Calculation Results

Relevant staff carried out field measurements of the typical drains studied in this paper from 11:00 to 14:00 on 29 August 2019. The instantaneous flow was $227.68 \text{ m}^3/\text{s}$. The water level on the left bank in front of the gate was 147.00 m and the water depth was 8.20 m; The water level on the right bank in front of the gate was 146.90 m and the water depth was 8.18 m. When measuring the velocity of the aqueduct on site, the first cross section of the aqueduct along the water flow direction was section A and the second cross section was section B. Measuring points were arranged along the right side of section A; 1 measuring point was arranged every 1 m, 12 measuring points were arranged in each channel body, and a total of 24 measuring points were arranged in the two tanks. The arrangement of the measuring points is shown in Figure 4.

Simulation parameters were set according to the analysis of the measured data. The measured flow was $227.68 \text{ m}^3/\text{s}$. The inlet flow boundary was set with a flow of $227.68 \text{ m}^3/\text{s}$. The water level at the outlet pressure boundary was 146.33 m. The initial water level of the model was 146.33 m. The initial velocity was 0.8 m/s. The channel roughness was set at 0.014. The calculation time was set to 5000 s. The initial time step was set to 0.002 s, and the minimum time step was set to 1×10^{-8} s. This paper selected the RNG $k-\epsilon$ turbulence model.

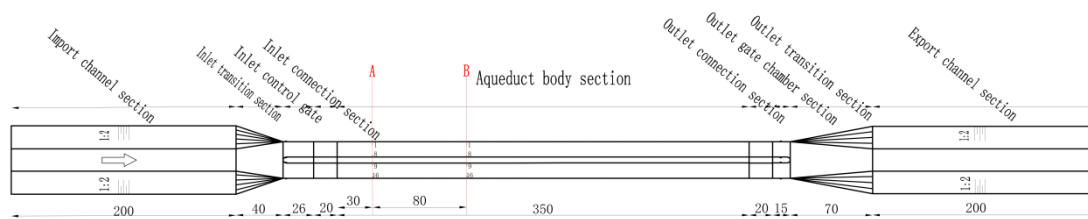


Figure 4. Layout of measuring points on a typical aqueduct.

It can be seen from the comparison between the measured water depth and the simulated water depth on the left and right banks of the aqueduct in Tables 2 and 3 that the water depth at different positions in the aqueduct body fluctuated, indicating that the numerical simulation could reflect the actual situation. The maximum difference in water depth was 0.07 m and the percentage of error in the measured water depth was 1.2%, which was consistent with the trend of the measured water depth data. By comparing the measured water depth and velocity with those of the numerical simulation, it could be seen that the parameter values and the numerical model establishment and solution results were reliable.

Table 2. Comparison between measured water depth and simulated water depth on the left bank of the aqueduct.

| Left Bank Section of Aqueduct Body Section | | | | | | |
|--|------|------|------|------|------|------|
| Measuring point | L1 | L2 | L3 | L4 | L5 | L6 |
| Measured water depth | 5.63 | 5.7 | 5.78 | 5.71 | 5.62 | 5.77 |
| Simulated water depth | 5.58 | 5.68 | 5.75 | 5.75 | 5.67 | 5.71 |
| Measuring point | L7 | L8 | L9 | L10 | L11 | L12 |
| Measured water depth | 5.64 | 5.78 | 5.74 | 5.77 | 5.63 | 5.70 |
| Simulated water depth | 5.58 | 5.73 | 5.68 | 5.71 | 5.72 | 5.76 |

Table 3. Comparison between measured water depth and simulated water depth on the right bank of the aqueduct.

| Right Bank Section of Aqueduct Body Section | | | | | | |
|---|------|------|------|------|------|------|
| Measuring point | R1 | R2 | R3 | R4 | R5 | R6 |
| Measured water depth | 5.65 | 5.77 | 5.80 | 5.71 | 5.74 | 5.65 |
| Simulated water depth | 5.60 | 5.70 | 5.74 | 5.76 | 5.69 | 5.61 |
| Measuring point | R7 | R8 | R9 | R10 | R11 | R12 |
| Measured water depth | 5.79 | 5.66 | 5.74 | 5.80 | 5.64 | 5.77 |
| Simulated water depth | 5.73 | 5.62 | 5.68 | 5.75 | 5.7 | 5.69 |

3.2. Setting of Simulated Working Conditions

In this paper, the study was carried out on the inlet tapering section of the aqueduct, and a three-dimensional numerical model of the inlet tapering section of the aqueduct was constructed as in Figure 5 without affecting the accuracy of the numerical simulation. A value of 200 m was taken for the upstream open channel section of the inlet tapering section, and 200 m was taken for the downstream channel body section of the tapering section.

As shown in Table 4, this paper considered the influence of the bottom width ratio of the inlet and outlet of the inlet and outlet tapering sections, and set a total of six model conditions; the simulation types included inlet $W_{up}/W_{down} < 1$, model number 1–4; $W_{up}/W_{down} = 1$, model number 5; and $W_{up}/W_{down} > 1$, model number 6. The model conditions were selected to reflect the influence of W_{up}/W_{down} on the overflow capacity. The water level and flow rate of each model condition were set as shown in Table 5, and eight water level and flow rates are set for each model condition.

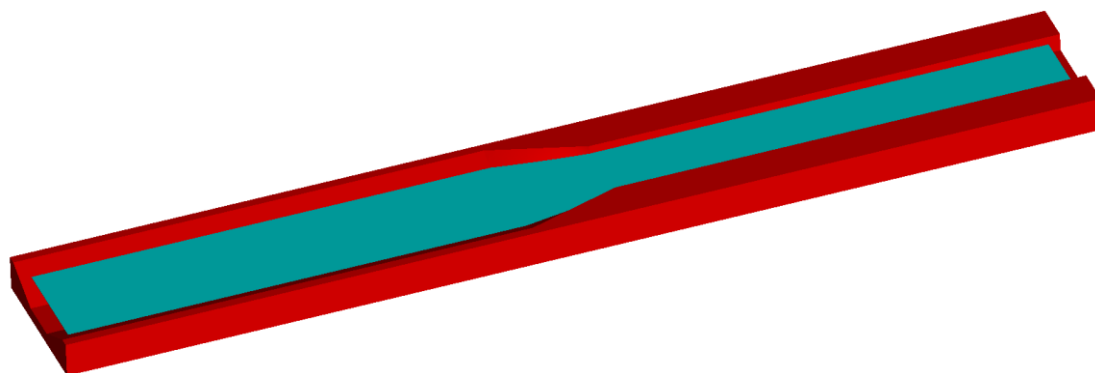


Figure 5. Prototype inlet gradient section model diagram.

Table 4. Values of W_{up} and W_{down} for the models' working conditions.

| Model Number | W_{up} (m) | W_{down} (m) | Model Number | W_{up} (m) | W_{down} (m) |
|--------------|--------------|----------------|--------------|--------------|----------------|
| 1 | 19 | 31 | 4 | 28 | 31 |
| 2 | 22 | 31 | 5 | 31 | 31 |
| 3 | 25 | 31 | 6 | 34 | 31 |

Table 5. Simulated water level for each operating condition (expressed as pressure).

| Work Conditions | Inlet Pressure P_{in} (m) | Outlet Pressure P_{out} (m) | Work Conditions | Inlet Pressure P_{in} (m) | Outlet Pressure P_{out} (m) |
|-----------------|-----------------------------|-------------------------------|-----------------|-----------------------------|-------------------------------|
| 1 | 4.8 | 4.5 | 5 | 6.8 | 6.5 |
| 2 | 5.3 | 5.0 | 6 | 7.3 | 7.0 |
| 3 | 5.8 | 5.5 | 7 | 7.8 | 7.5 |
| 4 | 6.3 | 6.0 | 8 | 8.3 | 8.0 |

4. Analysis of Simulation Results

In the energy equation, asymptotic section head loss is mainly local head loss; this study did not consider the head loss along the asymptotic section to calculate the local head loss. According to the simulation results, we could derive the upstream and downstream overwater area of the inlet gradient section, as well as derive the water surface contraction angle θ (the angle between the edge of the water surface at the transition section and the centerline). The model working condition was $W_{up} = 19$ m and $W_{down} = 31$ m, and the simulation working condition 1 results are shown in Table 6.

Table 6. Weir head under simulated working conditions.

| Water Level (m) | Angle ($^{\circ}$) | Water Depth of Tank (m) | Downstream Area (m^2) | Upstream Water Depth (m) | Upstream Area (m^2) | Head Loss Coefficient |
|-----------------|----------------------|-------------------------|---------------------------|--------------------------|-------------------------|-----------------------|
| 8.3 | 14.84 | 6.184 | 191.704 | 8.220 | 291.291 | 0.280 |
| 7.8 | 13.5 | 5.695 | 176.542 | 7.724 | 266.081 | 0.311 |
| 7.3 | 12.13 | 5.194 | 161.002 | 7.221 | 241.485 | 0.339 |
| 6.8 | 10.76 | 4.705 | 145.867 | 6.729 | 218.392 | 0.383 |
| 6.3 | 9.37 | 4.206 | 130.374 | 6.225 | 195.789 | 0.420 |
| 5.8 | 7.97 | 3.715 | 115.168 | 5.732 | 174.615 | 0.464 |
| 5.3 | 6.56 | 3.225 | 99.963 | 5.236 | 154.331 | 0.527 |
| 4.8 | 5.14 | 2.750 | 85.241 | 4.745 | 135.193 | 0.593 |

As can be seen above, Nguyen et al. experimentally determined the head loss coefficient of a rectangular open channel to a rectangular abruptly constricted pressurized pipe. A head loss coefficient of $\zeta = 0.63 (1 - A_{down}/A_{up})$ was obtained, and A_{up} and A_{down} were

the upstream and downstream cross-sectional over-water areas, respectively. Tokyay fitted the local head loss expression $\zeta = 0.74(\Delta z/h_1)^{0.5}$ for a 45° inclined negative step flow via an experimental study; h_1 was the downstream water depth and Δz was the difference in the elevation of the bottom surface of the inlet gradient section. In this paper, through the analysis of the simulation results and taking into account the effects of the water surface contraction angle and the upstream and downstream cross-sectional areas of the gradient section, the expression of the head loss coefficient of the gradient section can be given on the basis of existing research [5].

$$\zeta = \frac{\theta}{90} \left(1 - \frac{A_{down}}{A_{up}} \right)^{x_1} + x_2(\Delta z/h_1)^{x_3} \tag{5}$$

Substituting the results of $W_{up}/W_{down} = 19/31$ simulated working conditions into Equation (5), we get: coefficients $x_1 = 20.755$, $x_2 = 0.837$, and $x_3 = 0.891$, and the correlation coefficient is 0.995.

As shown in Table 7, the simulation results of each model condition were analyzed.

Table 7. Weir head under the simulated working conditions.

| W_{up}/W_{down} | Angles (°) | Local Head Loss Coefficient | W_{up}/W_{down} | Angles (°) | Local Head Loss Coefficient | W_{up}/W_{down} | Angles (°) | Local Head Loss Coefficient |
|-------------------|------------|-----------------------------|-------------------|------------|-----------------------------|-------------------|------------|-----------------------------|
| 19/31 | 14.84 | 0.280 | 22/31 | 16.83 | 0.249 | 25/31 | 18.78 | 0.222 |
| | 13.5 | 0.311 | | 15.51 | 0.273 | | 17.48 | 0.247 |
| | 12.13 | 0.339 | | 14.17 | 0.292 | | 16.17 | 0.263 |
| | 10.76 | 0.383 | | 12.82 | 0.323 | | 14.84 | 0.292 |
| | 9.37 | 0.420 | | 11.45 | 0.357 | | 13.5 | 0.319 |
| | 7.97 | 0.464 | | 10.07 | 0.400 | | 12.13 | 0.358 |
| | 6.56 | 0.527 | | 8.67 | 0.451 | | 10.76 | 0.406 |
| | 5.14 | 0.593 | | 7.27 | 0.513 | | 9.37 | 0.468 |
| 28/31 | 20.68 | 0.211 | 31/31 | 22.54 | 0.201 | 34/31 | 24.35 | 0.191 |
| | 19.42 | 0.232 | | 21.31 | 0.223 | | 23.15 | 0.217 |
| | 18.13 | 0.246 | | 20.05 | 0.236 | | 21.92 | 0.227 |
| | 16.83 | 0.281 | | 18.78 | 0.262 | | 20.68 | 0.255 |
| | 15.51 | 0.298 | | 17.48 | 0.284 | | 19.42 | 0.272 |
| | 14.17 | 0.335 | | 16.17 | 0.323 | | 18.13 | 0.310 |
| | 12.82 | 0.380 | | 14.84 | 0.364 | | 16.83 | 0.350 |
| | 11.45 | 0.440 | | 13.5 | 0.424 | | 15.51 | 0.410 |

As shown in Figure 6, the local head loss coefficient of each model condition decreased with the increase in the water surface contraction angle, and the local head loss coefficient corresponding to the same water surface contraction angle also increased with the increase in W_{up}/W_{down} . The water surface contraction angle θ (°) and the local head loss coefficient had a good exponential function relationship that met $\zeta = \alpha e^{\beta(W_{up}/W_{down})}$, where α and β are the formula coefficient terms and the correlation coefficients R^2 of each model condition fit were above 0.98.

As shown in Figure 7, the nonlinear regression analysis of W_{up}/W_{down} with exponential function $\zeta = \alpha e^{\beta(W_{up}/W_{down})}$ was performed for each model working condition. W_{up}/W_{down} had a good one-to-one quadratic function relationship with coefficient α , and the correlation coefficient R^2 was 0.9996; W_{up}/W_{down} had a good one-to-one quadratic function relationship with coefficient β , and the correlation coefficient R^2 was 0.9577.

Through the above analysis, the local head loss coefficient of the inlet tapering section of the aqueduct was written as an exponential function relationship, $\zeta = \alpha e^{\beta(W_{up}/W_{down})}$, related to the water surface contraction angle in the tapering section, and coefficients α , β , and W_{up}/W_{down} had a one-dimensional quadratic function relationship. In order to verify the accuracy and applicability of the formula, the formula was used to solve the local head loss coefficient when W_{up}/W_{down} was 19/31 and the water surface contraction angle was 10.76°. The formula calculated the local head loss coefficient to be 0.3796, the simulated value was 0.383, the error was 3.4×10^{-3} , and the error percentage was 0.89%.

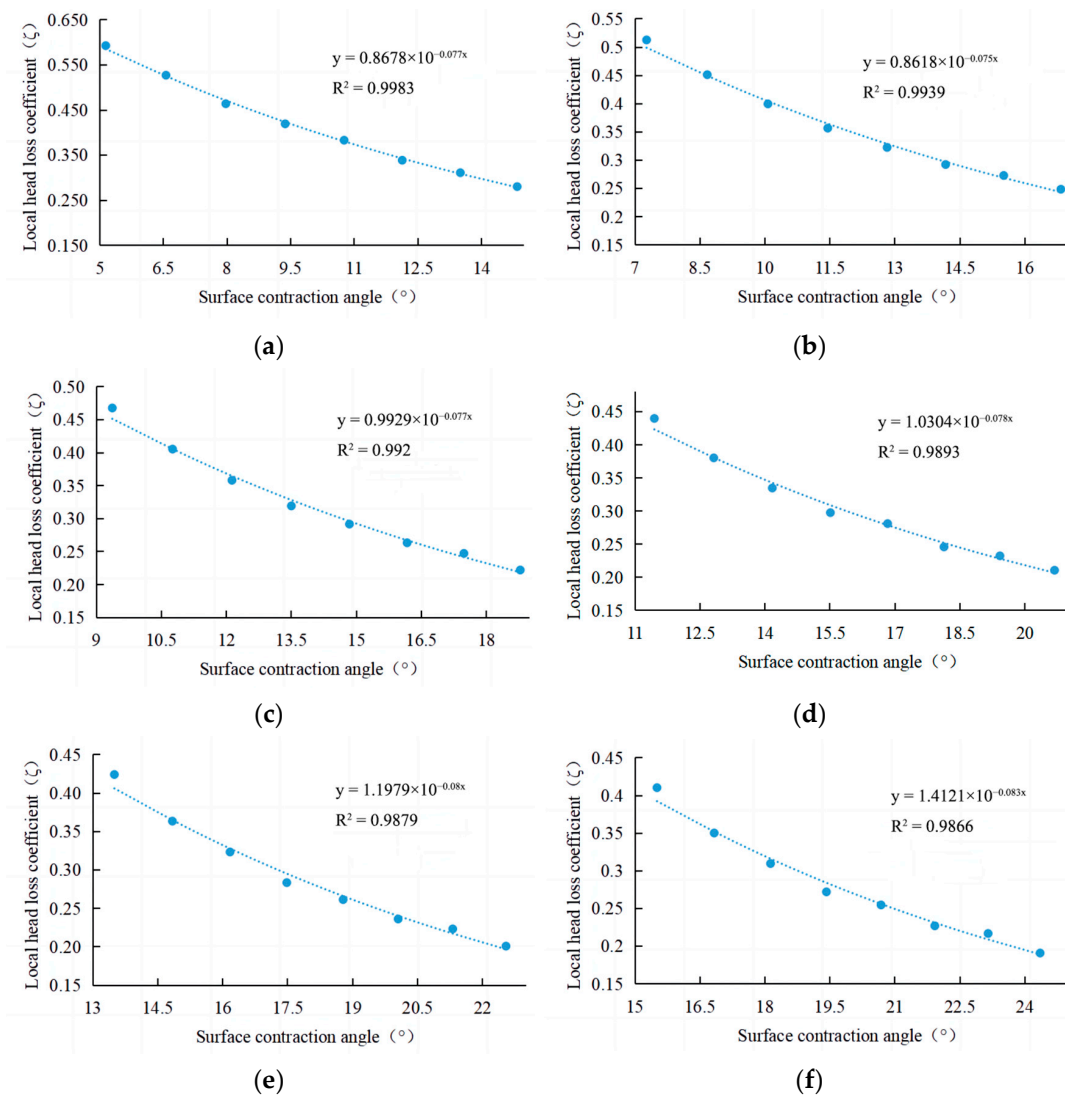


Figure 6. Each model working condition water surface contraction angle as a function of the local head loss coefficient. (a) θ as a function of ζ at $W_{up}/W_{down} 19/31$; (b) θ as a function of ζ at $W_{up}/W_{down} 22/31$; (c) θ as a function of ζ at $W_{up}/W_{down} 25/31$; (d) θ as a function of ζ at $W_{up}/W_{down} 28/31$; (e) θ as a function of ζ at $W_{up}/W_{down} 31/31$; (f) θ as a function of ζ at $W_{up}/W_{down} 34/31$.

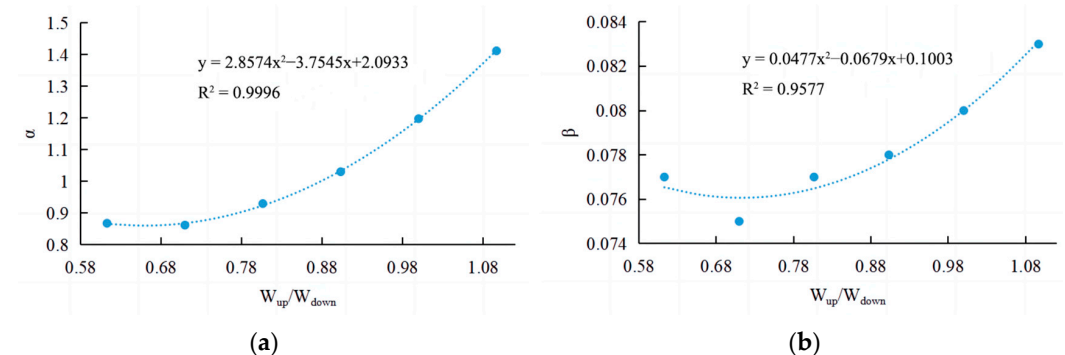


Figure 7. W_{up}/W_{down} as a function of coefficient. (a) W_{up}/W_{down} as a function of coefficient α ; (b) W_{up}/W_{down} as a function of coefficient β .

5. Conclusions

In this paper, the following conclusions were obtained from a three-dimensional simulation study of a typical aqueduct.

- (1) After the shape of the inlet tapering section was determined, the head loss coefficient ζ was related to the area of the overwater section of the inlet and outlet of the tapering section, the contraction angle of the water surface of the tapering section, and the difference in elevation of the bottom surface of the inlet and outlet of the tapering section. On the basis of existing research results, the local head loss coefficient was provided to meet the functional form of $\zeta = \frac{\theta}{90} \left(1 - \frac{A_{\text{down}}}{A_{\text{up}}}\right)^{x_1} + x_2(\Delta z/h_1)^{x_3}$, where x_1 , x_2 , and x_3 are the formula's coefficients.
- (2) The study and analysis of different bottom widths $W_{\text{up}}/W_{\text{down}}$ of the inlet gradient section showed that the local head loss coefficient decreased with the increase in the water surface contraction angle, and with the increase in $W_{\text{up}}/W_{\text{down}}$, the local head loss coefficient corresponding to the same water surface contraction angle also increased; the local head loss coefficient had a good exponential function relationship with $W_{\text{up}}/W_{\text{down}}$, which satisfied the functional form $\zeta = \alpha e^{\beta(W_{\text{up}}/W_{\text{down}})}$, where α and β are the formula's coefficients.

6. Patents

This section is not mandatory but may be added if there are patents resulting from the work reported in this manuscript.

Author Contributions: Conceptualization, H.Z. and S.Z.; writing—original draft preparation, J.C.; writing—review and editing, Y.T. All authors have read and agreed to the published version of the manuscript.

Funding: This paper was supported by the National Natural Science Foundation of China (Grant No. U22A20237) and the Open Research Fund of the Key Laboratory of Sediment Science and Northern River Training, the Ministry of Water Resources, China Institute of Water Resources and Hydropower Research (Grant No. IWHR-SED-202103).

Data Availability Statement: Data and materials are available from the corresponding author upon request.

Conflicts of Interest: The authors declare no conflict of interest.

References

1. Wang, Z. Von Karman and Karman Vortex Street. *Nat. J.* **2010**, *32*, 243–245.
2. Li, W. *Hydraulic Calculation Manual*, 2nd ed.; Water Conservancy and Hydropower Press: Beijing, China, 2006.
3. SL 482-2011; Specification for the Design of Irrigation and Drainage Canal System Buildings. Ministry of Water Resources of the People's Republic of China: Beijing, China, 2011.
4. Zhai, Y. Study on the calculation method of local head loss in the gradual change section of the main trunk canal of the South-North Water Diversion Project. *J. Irrig. Drain.* **2007**, *26* (Suppl. S1), 20–22. [\[CrossRef\]](#)
5. Wu, Y.Y.; Liu, Z.W.; Chen, Y.C. Flow characteristics and minor losses in transition section from trapezoidal open channel to horseshoe-shaped tunnel. *J. Hydroelectr. Eng.* **2016**, *35*, 46–55.
6. Wang, S. *Study on Water Level Fluctuation Mechanism and Control Measures of Large Aqueduct in Middle Route Project of South to North Water Diversion*; North China University of Water Resources and Electric Power: Zhengzhou, China, 2021. [\[CrossRef\]](#)
7. Qu, Z.; Lim, Z. Causal analysis on water level abnormal fluctuation in aqueduct and improvement measures: case of Lihe aqueduct in Middle Route of South to North Water Transfer Project. *Yangtze River* **2022**, *53*, 189–194. [\[CrossRef\]](#)
8. Kazemipour, A.K.; Apelt, C.J. *Resistance to Flow in Irregular Channels*; Department of Civil Engineering, University of Queensland: Brisbane, Australia, 1980.
9. Henderson, F.M. *Open Channel Flow*; McMillan Book Company: New York, NY, USA, 1966.
10. Chow, V.T. *Open-Channel Hydraulics*; McGraw-Hill: New York, NY, USA, 1959.
11. Yaziji, H.M. *Open-Channel Contractions for Subcritical Flow*; The University of Arizona: Tucson, AZ, USA, 1968.
12. Zhang, Z. *Hydraulic Design of the Inlet and Outlet Connection Section of a Pressureless Tunnel*; Shanxi Water Resources: Xi'an, China, 1991; pp. 34–40.
13. Gaetano, C.; David, D.; Corrado, G.; Michael, P. Hydraulic Capacity of Bend Manholes for Supercritical Flow. *J. Irrig. Drain. Eng.* **2023**, *149*, 04022048.
14. Cheng, Y.; Song, Y.; Liu, C.; Wang, W.; Hu, X. Numerical Simulation Research on the Diversion Characteristics of a Trapezoidal Channel. *Water* **2022**, *14*, 2706. [\[CrossRef\]](#)

15. Tellez-Alvarez, J.; Gómez, M.; Russo, B.; Amezaga-Kutija, M. Numerical and Experimental Approaches to Estimate Discharge Coefficients and Energy Loss Coefficients in Pressurized Grated Inlets. *Hydrology* **2021**, *8*, 162. [[CrossRef](#)]
16. Qi, L.; Chen, H.; Fei, W.; Dong, L. Three-dimensional numerical simulations of flows over spillway dam using accurate river terrain. *J. Hydroelectr. Eng.* **2016**, *35*, 12–20.
17. Wang, Y.; Bao, Z.; Wang, B. Three-dimensional numerical simulation of flow in stilling basin based on Flow-3D. *Eng. J. Wuhan Univ.* **2012**, *45*, 454–457+476.
18. Ran, D.; Wang, W.; Hu, X.; Shi, L. Analyzing hydraulic performance of trapezoidal cutthroat flumes. *Adv. Water Sci.* **2018**, *29*, 236–244.
19. Xiao, Y.; Wang, W.; Hu, X. Numerical simulation of hydraulic performance for portable short-throat flume in field based on FLOW-3D. *Trans. Chin. Soc. Agric. Eng.* **2016**, *32*, 55–61.
20. Guan, G.; Huang, Y.; Xiong, J. Uniform flow rate calibration model for flat gate under free-submerged orifice flow. *Trans. Chin. Soc. Agric. Eng.* **2020**, *36*, 197–204.

Disclaimer/Publisher's Note: The statements, opinions and data contained in all publications are solely those of the individual author(s) and contributor(s) and not of MDPI and/or the editor(s). MDPI and/or the editor(s) disclaim responsibility for any injury to people or property resulting from any ideas, methods, instructions or products referred to in the content.